Increasing Accuracy in Image-Guided Robotic Surgery Through Tip Tracking and Model-Based Flexion Correction

Ryan A. Beasley, *Member, IEEE*, and Robert D. Howe, *Senior Member, IEEE*

***Abstract*—Robot assistance can enhance minimally invasive image-guided surgery, but flexion of the thin surgical instrument shaft impairs accurate control by creating errors in the kinematic model. Two controller enhancements that can mitigate these errors are improved kinematic models that account for flexing and direct measurement of the instrument tip's position. This paper presents an experiment quantifying the benefits of these enhancements in an effort to inform development of an image-guided robot control system accurate in the presence of quasi-static instrument flexion. The study measured a controller's ability to guide a flexing instrument along user-commanded motions while preventing incursions into a forbidden region virtual fixture. Compared with the controller using neither enhancement, improved kinematics and reduced maximum incursion depth into the forbidden region by 28%, tip tracking by 67%, and both enhancements together by 83%.**

***Index Terms*—Flexible structures, modeling, quasi-static, surgery.**

I. Introduction

THE INCORPORATION of 3-D medical image data can enhance outcomes in many surgical procedures. In typical image-guidance implementations, the locations of pathologies are identified in preoperative computed tomography (CT) or MR images and surgical instruments are then directed to these locations, thereby minimizing damage to adjacent healthy tissue. This approach has become the standard of care in a number of orthopedic and neurosurgical procedures, and applications are developing in other surgical specialties. The integration of surgical robotics can further enhance this approach by taking advantage of the robot's ability to quickly and precisely move instruments to the target locations identified in the 3-D images [1]–[10]. Image-guided robotic surgery relies on the robot's ability to accurately move the instruments to specified positions in patient coordinates, and is therefore dependent on the accuracy of the robot controller and its kinematic model of the instrument.

Manuscript received February 26, 2008; revised September 8, 2008. First published February 27, 2009; current version published April 3, 2009. This paper was recommended for publication by Associate Editor C. Cavusoglu and Editor F. Park upon evaluation of the reviewers' comments. This work was supported in part by the National Science Foundation (NSF) under Grant EEC-9731748.

R. A. Beasley is with Texas A&M University, College Station, TX 77843 USA (e-mail: beasley@entc.tamu.edu).

R. D. Howe is with the Harvard School of Engineering and Applied Sciences and the Harvard–MIT Division of Health Sciences and Technology, Cambridge, MA 02138 USA (e-mail: howe@deas.harvard.edu).

Color versions of one or more of the figures in this paper are available online at http://ieeexplore.ieee.org.

Digital Object Identifier 10.1109/TRO.2009.2014498

Positioning errors occur when instrument geometry changes in response to interaction forces between the instrument and the surgical site. For example, in robot-assisted coronary artery bypass graft surgery, the internal mammary artery is harvested from the interior chest wall using blunt dissection and electrocautery [11], [12]. The forces generated by tissue interactions at the instrument tip can result in bending deflections of several millimeters, which is approximately the diameter of the target artery [7], [13]. This can eliminate the benefit of using preoperative images for optimizing port placement or implementing augmented reality and virtual fixtures for guidance [14]–[16].

The problem of instrument deflection occurs across a range of surgical procedures. One common task that causes bending is blunt dissection, which is a preferred method for separating tissues in minimally invasive surgery as it minimizes the risk of bleeding. Instrument tip forces of 8.5 N peak and 1.6 N rms have been measured for blunt dissection in laparoscopic surgical tasks [17]. Additionally, instrument handle forces during various laparoscopic tissue manipulation tasks have been measured with a mean of 8.5 N [18]. Resulting deflections can be quite significant; for example, applying a 1 N force to the tip of a typical thin surgical robot instrument results in a 15 mm tip deflection (straight endograspers for the ZEUS Surgical Robot System, Computer Motion, Inc; Goleta, CA; stainless steel shaft 355 mm long, 3.4 mm outer diameter, 1.5 mm inner diameter). Euler–Bernoulli calculations predict a tip deflection of 11.8 mm, where the 3.2 mm discrepancy is likely due to manufacturing imperfections and simplifications implicit in the model calculations. This problem will be increasingly limiting as thinner instruments are introduced over time to reduce damage to healthy tissue and access smaller anatomical targets, such as in robot-assisted sinus, intracardiac, pediatric, and fetal procedures [19]–[23].

Instrument deflections cause the robot controller to calculate the instrument tip's position from invalid forward kinematics. The controller then moves the robot's joints according to incorrect inverse kinematics or according to a Jacobian calculated from the incorrect kinematics. Such motions may be in undesired directions and thereby reduce patient safety [24]. Surgeons can compensate for such errors using visual feedback in teleoperated procedures, but such compensation may increase mental workload. Furthermore, surgeons cannot compensate when the robot motions are based on preoperative image information and executed in autonomous or semiautonomous modes such as when virtual fixtures are used to protect vital structures.

1552-3098/$25.00 © 2009 IEEE

Authorized licensed use limited to: Harvard University SEAS. Downloaded on July 8, 2009 at 15:59 from IEEE Xplore. Restrictions apply.

Previous research has developed two approaches toward reducing these errors: measuring the tip position and improving the kinematic model. Measuring the tip position using computer vision techniques [25]–[31] or electromagnetic sensors [32]–[35] bypasses the invalid forward kinematics, but such measurements do not directly reduce errors in the inverse kinematics. Metrics have been developed to evaluate the convergence properties of controllers that use tip tracking with incorrect inverse kinematics, but metrics alone do not reduce the motion errors [36]–[38]. To minimize errors in motion, the kinematics of flexible structures have been previously investigated, usually in an effort to identify the modes of dynamic flexion [39], [40]. Such dynamic flexion is not experienced by instruments in laparoscopic surgery because motions are slow and the instruments are in contact with a viscoelastic environment. Instrument flexion is therefore quasi-static. Aside from the authors' work on discretely loaded instruments, the only quasi-static flexion research on such tools has been for continuous load cases such as needle driving [41]–[43]. The research of Abolhassani *et al.* [44] is of particular interest as it uses real-time measurements to model the needle deflection, but the approach uses incremental updates to the model that are not applicable to loading conditions typical in laparoscopy and thoracoscopy [44].

The goal of this paper is to develop an image-guided robot control system that is accurate in the presence of quasi-static instrument flexion caused by interaction forces at the instrument tip. Previously, we have investigated 2-D quasi-static motions in experiments and simulations using a controller based on a quasi-static flexion model [24]. In that paper, the controller utilized measurements of the instrument tip's position and orientation to model and then move the instrument. The controller's performance has not been evaluated with respect to image guidance, nor has the benefit from the proposed model been separated from, and compared with, the benefit from tip tracking. This paper investigates the separate benefits from more accurate kinematics and from directly measuring the position of the instrument tip. To that end, subjects executed a 3-D teleoperation task while relying on guidance from virtual fixtures. The task produced instrument flexion due to interaction with a silicone tissue model. The subjects performed the same task with multiple controllers, and the experimental results evaluate the controllers' image-guided performances by measuring incursions into the forbidden region virtual fixture. The findings are applicable to systems where positioning accuracy is important in the presence of quasi-static flexion, such as robotic surgery.

II. Methods

In image-guided robotic surgery, the robot is coupled to the surgical instruments, typically at a wrist (Fig. 1). As in many laparoscopic and thoracoscopic procedures, we assume that the surgical instruments are introduced into the patient's body through *endoscopic ports*, rigid cannulae a few centimeters in length that are tightly inserted into small incisions. In addition to the instruments, an *endoscope* may be inserted into the patient to provide visual feedback.

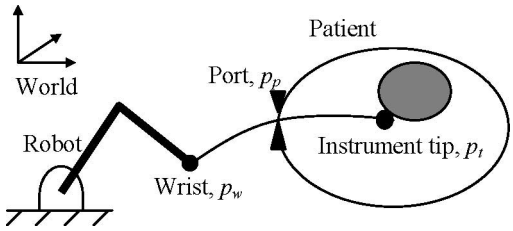

Fig. 1. Interaction forces on tip of minimally invasive surgical instrument shaft cause shaft flexion.

The preoperative image data is first registered to the patient's anatomy to establish the coordinate transform between the image data and the robot's world frame. In teleoperated image-guided robotic surgery, the surgeon observes the endoscopic image as well as preoperative image-based overlays or virtual fixtures and establishes the desired instrument positions by manipulating handles at the surgeon's console. In (semi-)autonomous robotic surgery, the robot follows the preplanned instrument trajectory. In both cases, the robot positions the instruments in a world coordinate frame using motor torques commanded by the controller. Interaction forces between the instrument tip and the surgical site cause instrument flexion.

This paper investigates the positioning accuracies of four controllers in the presence of this quasi-static instrument flexion. In this study, human subjects perform a teleoperation task under the guidance of virtual fixtures. Incursions into the virtual fixture are used to measure the accuracy of the controllers, while the human subjects provide unscripted motions under the guidance of visual feedback, as expected in the operating room.

A. Controller Design

Fig. 2 depicts the instrument control used in this paper. The premise is that the existing joint level controller accepts a desired wrist position and that the robot arm can precisely position the wrist; this avoids changes to the existing low-level robot control system to minimize the regulatory certification process. The desired wrist position $p_{w,\mathrm{desired}}$ is calculated as a motion from $p_w = (x_w, y_w, z_w)$, the current wrist position, based on the intended change in the instrument tip position, Δp_t. $p_{w,\mathrm{desired}}$ can be expressed as

$$p_{w,\mathrm{desired}} = p_w + \Delta p_w \cong p_w + J_i^{-1}\Delta p_t \tag{1}$$

$$\Delta p_t = p_{t,\mathrm{desired}} - p_t \tag{2}$$

where $p_{t,\mathrm{desired}}$ is the desired tip position in world coordinates, $p_t = (x_t, y_t, z_t)$ is the current tip position in world coordinates, Δp_w is the desired wrist motion, and J_i is the instrument Jacobian relating motions of the robot's wrist to motions of the instrument tip

$$J_i = \begin{bmatrix} \dfrac{\partial x_t}{\partial x_w} & \dfrac{\partial x_t}{\partial y_w} & \dfrac{\partial x_t}{\partial z_w} \\ \dfrac{\partial y_t}{\partial x_w} & \dfrac{\partial y_t}{\partial y_w} & \dfrac{\partial y_t}{\partial z_w} \\ \dfrac{\partial z_t}{\partial x_w} & \dfrac{\partial z_t}{\partial y_w} & \dfrac{\partial z_t}{\partial z_w} \end{bmatrix}. \tag{3}$$

Authorized licensed use limited to: Harvard University SEAS. Downloaded on July 8, 2009 at 15:59 from IEEE Xplore. Restrictions apply.

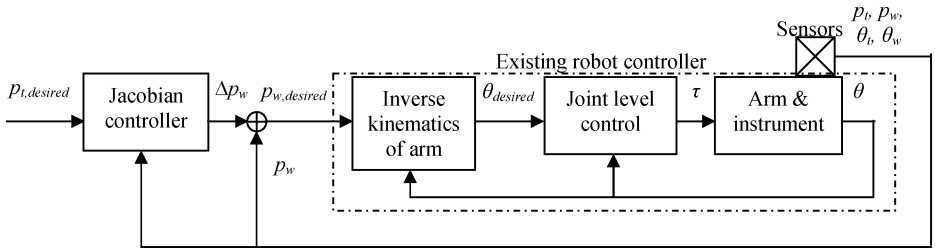

Fig. 2. Proposed controller consists of inner and outer feedback loops. The inner loop moves the robot's wrist to a desired position and is assumed to be a preexisting part of the surgical robot. The proposed outer loop is Jacobian-based, using measurements of the tip position (p_t), tip orientation (θ_t), wrist position (p_w), and wrist orientation (θ_w) to calculate the desired position of the wrist.

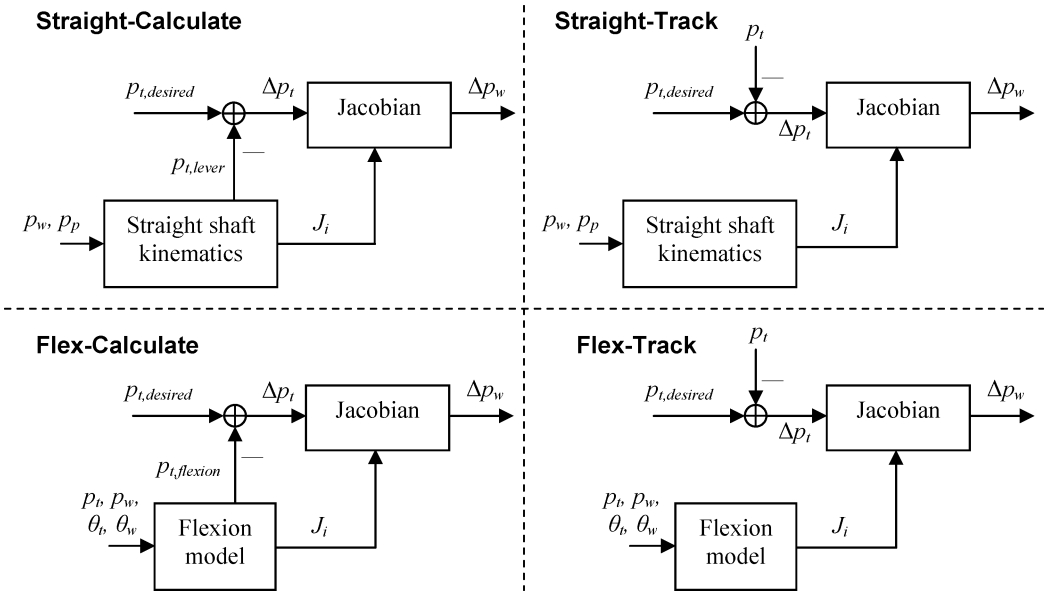

Fig. 3. Four Jacobian-based calculations of the desired wrist motion were compared to evaluate the benefits of tip tracking and a more accurate kinematic model. Each calculation has a two-word name signifying the shaft model used to calculate the Jacobian (straight shaft or flexed shaft) and how the current tip position was determined (calculation or electromagnetic tracker).

Jacobian-based controllers are appealing because, when combined with tip tracking, the system converges to the desired position even in the presence of small kinematic errors [36]. In the same situation, inverse-kinematics-based controllers are not guaranteed to converge to the desired position without an additional method for correcting for the kinematic errors. The experiment described in this paper could be performed using an inverse kinematics controller, in which case tip tracking would be expected to provide less benefit.

Equation (1) contains the inverse of the Jacobian for the intuitive relationship between the positions at the two ends of the instrument. Traditional Jacobian-based controllers use the transpose Jacobian, but a recent study has shown that the two approaches are dual controllers [45], which means the inverse Jacobian in (1) can be replaced with the transpose Jacobian. The stability of the controller described in (1), (2), and Fig. 2 has been investigated in [24] and [36], which showed monotonic convergence in the presence of small errors in the Jacobian.

B. Four Jacobian-Based Controllers

Four Jacobian-based controllers were constructed to investigate the benefits of two separate enhancements, tip tracking, and more accurate kinematics (Fig. 3). All four controllers output a change in the wrist position while accepting as inputs the desired tip position and the current wrist position. Additionally, each controller accepts as inputs one or more of: the current tip position, the port position, and the orientations at the wrist and tip.

The first controller, "Straight-Calculate," did not use any measurements. This controller used the kinematics of a straight rod

$$p_{t,\text{lever}} = \frac{L\,(p_p - p_w)}{\|p_p - p_w\|} + p_w \tag{4}$$

where L is the length of the instrument shaft, and p_p, is the port position in world coordinates. The Jacobian is calculated by substituting (4) into (3). Since this controller does not receive measurements of the tip position, the desired tip motion is calculated by substituting (4) for the tip position p_t in (2). In (4), the port position in world coordinates is assumed known and constant throughout the controller update so that it is a constant in the Jacobian's derivative operation. The port position can be measured directly or inferred from instrument motions. The second controller, "Straight-Track," used the same Jacobian but used position measurements of the instrument's tip

Authorized licensed use limited to: Harvard University SEAS. Downloaded on July 8, 2009 at 15:59 from IEEE Xplore. Restrictions apply.

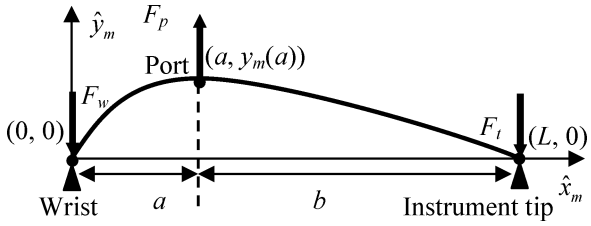

Fig. 4. Two models of the instrument shaft were used, a pinned–pinned beam (shown) and a straight link (not shown). These models were used to calculate the Jacobians and in calculations of the tip position.

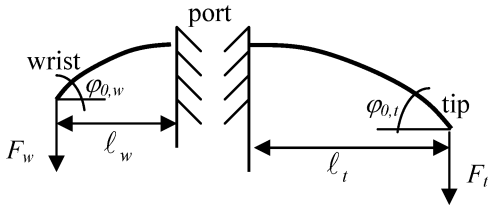

Fig. 5. Cantilever model for calculation of the wrist to tip distance for the flexed instrument shaft.

in (2) to determine the tip position error. The third controller, "Flex-Calculate," used a model of a flexing instrument to calculate both the Jacobian and the tip position. The fourth controller, "Flex-Track," used the flexion-model-based Jacobian with the tip error determined from tip position measurements.

C. Flexion Model

As the instrument tip interacts with tissue, tip forces orthogonal to the instrument axis generate reaction forces at the port and wrist. These forces result in bending of the instrument. To calculate the correct Jacobian, the goal is to determine the actual kinematics of the instrument, i.e. its shape as it flexes during the procedure. We use the Euler–Bernoulli beam bending equations to model the instrument shape. We assume no moments are applied to the instrument and forces are applied normal to the instrument at the wrist, port, and tip (Fig. 4). The flexed instrument therefore lies in a 2-D plane containing the wrist, port, and tip, and can be modeled as a pinned–pinned beam with a point load for the port force. This model precludes complicated shapes such as s-shaped curves and buckling due to axial loading, in the interest of low complexity. The accuracy of this model decreases as the instrument tip penetrates an object, so that the point load becomes a distributed load. This situation is accurate for tasks where the primary interaction is at the instrument tip, as in many laparoscopic and thoracoscopic procedures. Furthermore, the model accuracy decreases for situations combining flexion and axial forces large enough to cause buckling of the instrument. The following equations for instrument deflection can be readily modified to include distributed, and/or axial, loading if the details of the loading can be inferred during the procedure.

From [46], the height of the beam in model coordinates (Fig. 4) is

$$y_m(x_m) = \frac{F_p}{6EI}\left(Lbx_m\left(1 - \frac{b^2}{L^2} - \frac{x_m^2}{L^2}\right) + \langle x_m - a\rangle^3\right) \tag{5}$$

and the slope of the beam is

$$y'_m(x_m) = \frac{F_p}{6EI}\left(Lb\left(1 - \frac{b^2}{L^2} - \frac{3x_m^2}{L^2}\right) + 3\langle x_m - a\rangle^2\right) \tag{6}$$

where x_m is the x-coordinate in model space, a is the x-position of the port in model coordinates, F_p is the force at the port, L is the length of the beam, $b \equiv L - a$, E is Young's modulus, I is the cross-sectional moment of inertia, and

$$\langle x_m - a\rangle = \begin{cases} 0 & x_m \le a \\ (x_m - a) & x_m \ge a. \end{cases} \tag{7}$$

This model contains two parameters, F_p and a. We calculate these parameters from orientation measurements at the ends of the instrument,

$$F_p = \frac{2EI(y'_{m,\text{measured}}(0) - y'_{m,\text{measured}}(L))}{a(a-L)} \tag{8}$$

$$a = \frac{L(2y'_{m,\text{measured}}(L) + y'_{m,\text{measured}}(0))}{y'_{m,\text{measured}}(L) - y'_{m,\text{measured}}(0)} \tag{9}$$

where $y'_{m,\text{measured}}(x)$ is the slope of the instrument measured at a distance x from the wrist and then transformed from world space to model space.

D. Tip Position from Model

To calculate the tip position in world coordinates from the flexion model, as required by the Flex-Calculate controller, the tip position is transformed from model coordinates

$$p_{t,\text{flexion}} = x_{t,m}\hat{v}_x + y_{t,m}\hat{v}_y + p_w \tag{10}$$

where $x_{t,m}$ and $y_{t,m}$ are the x- and y-model coordinates for the tip, $\hat{v}_x$ is the model's x-axis in world coordinates, and $\hat{v}_y$ is the model's y-axis in world coordinates ($\hat{v}_z$ is not required because the model does not have any displacement along its z-axis). Thus, the vector from the wrist position to the calculated tip position is oriented using the measured tip position, but as a result of the flexion model's "small angle" assumption, the vector length is constant and equal to the length of the straight shaft. This assumption introduces errors into the calculated tip position because the actual distance between the instrument's endpoints varies as a function of the flexion. To improve the calculated tip position, the vector length was determined using large deflection equations following the method described in [47].

For this adjustment, the rod was modeled as two cantilever beams extending from either side of the port (Fig. 5). From the model parameters, the forces at the ends of those cantilevers are

$$F_w = \frac{F_p(L-a)}{L} \tag{11}$$

$$F_t = \frac{F_p a}{L}. \tag{12}$$

Authorized licensed use limited to: Harvard University SEAS. Downloaded on July 8, 2009 at 15:59 from IEEE Xplore. Restrictions apply.

The nondimensional load parameters for each side were

$$\alpha_w = \frac{F_w a^2}{2EI} \tag{13}$$

$$\alpha_t = \frac{F_t (L-a)^2}{2EI}. \tag{14}$$

Following [47], a precalculated lookup table that related the nondimensional load parameters to the angles at both ends of the cantilevers, $\varphi_{0,w}(\alpha_w)$ and $\varphi_{0,t}(\alpha_t)$, was used to reduce the number of calculations performed during each servo update. The table was constructed by solving

$$\alpha = \int_0^{\varphi_0} \frac{d\varphi}{4(\sin\varphi_0 - \sin\varphi)} \tag{15}$$

for values of φ_0 between 0 and 0.5. The adjusted distance from wrist to tip is then

$$L_{\text{cantilever}} = \ell_w + \ell_t \tag{16}$$

$$\ell_w = \sqrt{\sin(\varphi_{0,w})}\sqrt{\frac{2EI}{F_w}} \tag{17}$$

$$\ell_t = \sqrt{\sin(\varphi_{0,t})}\sqrt{\frac{2EI}{F_t}}. \tag{18}$$

The x-position of the rod's tip in flexion model coordinates is then

$$\begin{bmatrix} x_{t,m} \\ y_{t,m} \end{bmatrix} = L_{\text{cantilever}} \begin{bmatrix} \cos(\gamma) \\ \sin(\gamma) \end{bmatrix} \tag{19}$$

where the angle of rotation is determined from (6) and $y'_{m,\text{measured}}(0)$, the measured slope in model coordinates from

$$\gamma = \arctan\left(y'_{m,\text{measured}}(0)\right) - \arctan\left(y'_m(0)\right). \tag{20}$$

The adjusted tip position is calculated by substituting (19) into (10). For the experimental apparatus described later and based on the resolution of the tracking sensor, the approach described in (8) through (20) yields a worst case error of 0.1 mm.

E. Flexion Jacobian

Once the model parameters, F_p and a, have been estimated, the Jacobian relating the motions of the flexed instrument's endpoints can be calculated. First, a Jacobian is constructed to relate the 2-D motions within the plane of curvature. The tip position within the plane can be written as

$$\begin{bmatrix} x_{t,m} \\ y_{t,m} \end{bmatrix} = L \begin{bmatrix} \cos(\varphi) \\ \sin(\varphi) \end{bmatrix} + \begin{bmatrix} x_{w,m} \\ y_{w,m} \end{bmatrix} \tag{21}$$

$$\varphi = \arctan\left(\frac{y_{p,m} - y_{w,m}}{x_{p,m} - x_{w,m}}\right) - \arctan\left(\frac{y_m(a)}{a}\right) \tag{22}$$

where $p_{w,m} = (x_{w,m}, y_{w,m})$ is the x-position of the wrist in flexion model coordinates, and φ incorporates the port location, $p_{p,m} = (x_{p,w}, y_{p,m})$, which is the instrument's fulcrum and is assumed fixed in position during controller updates [and therefore, a constant in (23)]. Taking the partial derivatives according to

$$J_{2D} = \begin{bmatrix} \dfrac{\partial x_{t,m}}{\partial x_{w,m}} & \dfrac{\partial x_{t,m}}{\partial y_{w,m}} \\ \dfrac{\partial y_{t,m}}{\partial x_{w,m}} & \dfrac{\partial y_{t,m}}{\partial y_{w,m}} \end{bmatrix} \tag{23}$$

the 2-D Jacobian can be written as a function of $p_{w,m}$, $p_{p,m}$, a, and $y_m(a)$. After the derivative operations, the port position, $p_{p,m}$, is written as

$$\begin{bmatrix} x_{p,m} \\ y_{p,m} \end{bmatrix} = \begin{bmatrix} a \\ y_m(a) \end{bmatrix} \tag{24}$$

and from (5), the deflection height at the port in model coordinates can be written as

$$y_m(a) = \left(\frac{F_p}{EI}\right)\left(\frac{a^2(a-L)^2}{3L}\right). \tag{25}$$

Combining these equations permits calculation of the 2-D Jacobian in terms of F_p and a.

To create the 3-D Jacobian from the 2-D Jacobian, we consider infinitesimal motions orthogonal to the plane and assume they cause the instrument to pivot about the port without changing shape. Such motions rotate the plane about a line that passes through the port and that is orthogonal to the vector from wrist to tip. Therefore, infinitesimal orthogonal motions of either endpoint result in motions of the other endpoint that are also purely orthogonal to the plane. The scaling factor relating the magnitudes of the motions comes from the ratio of the instrument lengths on either side of the port. The resulting 3-D flexed instrument Jacobian is

$$J_i = R_m^{\text{world}} \begin{bmatrix} \dfrac{\partial x_{t,m}}{\partial x_{w,m}} & \dfrac{\partial x_{t,m}}{\partial y_{w,m}} & 0 \\ \dfrac{\partial y_{t,m}}{\partial x_{w.m}} & \dfrac{\partial y_{t,m}}{\partial y_{w,m}} & 0 \\ 0 & 0 & \dfrac{-(L-a)}{a} \end{bmatrix} \left(R_m^{\text{world}}\right)^{-1} \tag{26}$$

where

$$R_m^{\text{world}} = [\,\hat{v}_x \quad \hat{v}_y \quad \hat{v}_z\,] \tag{27}$$

$$\frac{\partial x_{t,m}}{\partial x_{w.m}} = 1 + \frac{L}{L_{\text{meas}}^2}(y_m(a) + a\kappa)\sin(\varphi) \tag{28}$$

$$\frac{\partial x_{t,m}}{\partial y_{w,m}} = \frac{L}{L_{\text{meas}}^2}(-a + y_m(a)\kappa)\sin(\varphi) \tag{29}$$

$$\frac{\partial y_{t,m}}{\partial x_{w,m}} = \frac{L}{L_{\text{meas}}^2}(y_m(a) + a\kappa)\cos(\varphi) \tag{30}$$

$$\frac{\partial y_{t,m}}{\partial y_{w,m}} = 1 - \frac{L}{L_{\text{meas}}^2}(a - y_m(a)\kappa)\cos(\varphi) \tag{31}$$

$$\kappa = \frac{(2a - L - 1)\, y_m(a)}{a + (2a - L)\, y_m^2(a)} \tag{32}$$

$$L_{\text{meas}} = \left(a^2 + y_m^2(a)\right)^{\frac{1}{2}}. \tag{33}$$

Authorized licensed use limited to: Harvard University SEAS. Downloaded on July 8, 2009 at 15:59 from IEEE Xplore. Restrictions apply.

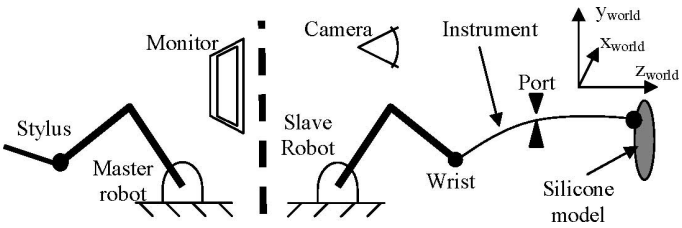

Fig. 6. Diagram of experimental setup. The subject teleoperates a robot holding an instrument shaft. The shaft is used to dig into one bed of silicone for each of the four Jacobian-based controllers. A virtual fixture attempts to limit incursion depth by restricting motions of the slave robot.

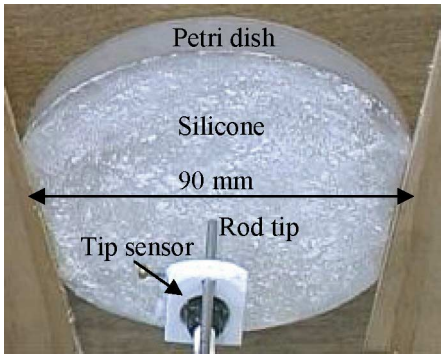

Fig. 7. Camera view of silicone and instrument tip with electromagnetic sensor.

F. Experimental Setup

The relative performance of kinematic bending models and tip tracking were evaluated in an experiment that used the teleoperated control mode with a simulated forbidden-region virtual fixture. Two small robots (Phantom Premium 1.5, Sensable Technologies; Woburn, MA, USA) were used in a surgeon/master and patient/manipulator setup similar to minimally invasive surgical robots (Fig. 6). (A surgical robot was not used due to the difficulty in accessing the proprietary controller on commercial systems.) The surgical target was modeled by a silicone rubber cylinder (RTV 6166, 3.4 kPa elastic modulus, General Electric; Fairfield, CT) in a Petri dish (90 mm diameter, 15 mm deep) (Fig. 7). The Petri dish was mounted facing the "patient"-side robot at a distance of 740 mm from the robot base axis. This setup emulates the use of a surgical robot used to perform blunt dissection of tissue under the guidance of virtual fixtures as in [7].

The instrument was a stainless steel rod (600 mm long, 2.38 mm diameter), held by the patient-side robot. This is roughly double the length and half the diameter of a typical laparoscopic or thoracoscopic instrument; the exaggerated dimensions enhance the bending effects to simplify evaluation of the controller's performance and to minimize the effects of the resolution limits of the sensors. The rod passed through a port, consisting of a hole (2.49 mm diameter, 26 mm long) in a Teflon block mounted on a low-friction gimbal placed 460 mm in front of the robot base joint axis.

Two electromagnetic position and orientation sensors (Minibird 800, Ascension Technologies; Burlington, VT, USA) were attached at the robot's wrist and 20 mm from the rod's tip. Electromagnetic trackers are frequently used in image-guided surgical procedures [6]. Tracker accuracy suffers as a result of the electromagnetic interference and high metal content of the operating room, but proper calibration can significantly reduce those errors and technological advances continue increasing the accuracy and noise rejection of the sensors [33], [34]. A recent study shows mean position errors of half a millimeter or less due to proximity of various surgical instruments [35].

Measurements from these sensors were acquired at 144 Hz for use in the controllers and flexion model. If the geometry of the instrument changed significantly between updates (approximately 7 ms), motion errors would result, requiring faster sensors to resolve. No evidence of such errors was evident in the trials. The measured rms noise in the experimental setup was 0.13 mm and 0.00056 rad. Motor activity had no measurable effect on the readings for either sensor. When servoing the instrument tip at a constant desired position in the center of the task workspace, the rms error in tip position was 0.16 mm for either of the controllers using tip tracking. No magnetic field calibration was performed that could further reduce errors due to noise.

On the "surgeon" side, the subject moved the stylus attached to the master robot while watching a monitor. The monitor displayed a close-up view of the silicone and the tip of the rod (Fig. 7). This view was recorded by a camera positioned 360 mm behind and 890 mm above the patient-side robot.

The desired position for the rod's tip $p_{t,\mathrm{desired}}$ was set to the master robot's position at the gimbal at the base of the stylus grasped by the subject. This desired position was adjusted by a forbidden-region virtual fixture [7], [8], which was in the form of a plane 6 mm beneath the surface of the silicone. Any desired tip positions deeper than this plane were projected onto the plane. The desired wrist position $p_{w,\mathrm{desired}}$ was calculated from this adjusted position using one of the four Jacobian-based controllers. The wrist was driven to this desired position using a proportional-derivative controller. The master controller motors were not activated, i.e., there was no active force feedback to the subject from the patient-side manipulator.

Subjects performed a task motivated by an image-guided minimally invasive blunt dissection task. Image guidance took the form of a forbidden region virtual fixture designed to limit penetration depth of the rod's tip into the silicone. Medical images (e.g., CT, MRI, or endoscopic images) can be used to position such virtual fixtures in relation to specific tissue locations. The robot controller then prevents the instrument from entering the areas protected by the virtual fixtures. As long as the tissue locations as depicted in the medical images are accurate, and the robot's controller is accurate, these limits prevent the instrument from interacting with the tissues at those locations, thereby increasing patient safety. In this task, as the rod's tip interacted with the silicone tissue model, the rod flexed, changing the kinematic parameters. The various controllers' performances are indicative of their performances in any task involving quasi-static flexion, such as minimally invasive robotic surgery.

Authorized licensed use limited to: Harvard University SEAS. Downloaded on July 8, 2009 at 15:59 from IEEE Xplore. Restrictions apply.

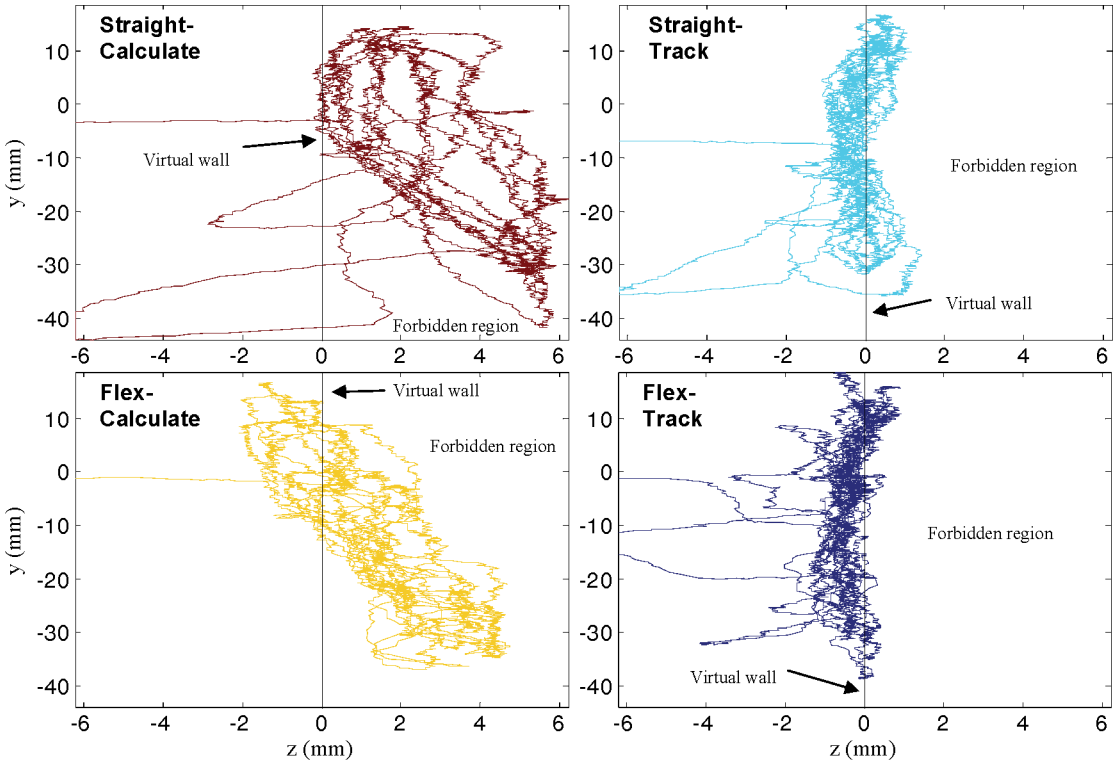

Fig. 8. Representative tip trajectories projected into the vertical plane. These trajectories are from the subject with the median maximum incursion depths, but are representative for all the subjects. The Flex-Track Jacobian enters the forbidden region to the least depth, followed by Straight-Track, then Flex-Calculate, and finally Straight-Calculate. The y and z axes use different scaling to show detail.

G. Protocol

Subjects were instructed to move the master robot such that the rod's tip moved around in the silicone, staying within an outline drawn on the monitor. As the tip moved in the silicone, the silicone's surface was visibly damaged. Subjects were told to keep the tip inserted as deeply as possibly into the silicone, and to attempt to damage as much of the silicone within the outline as possible. Subjects were informed that a virtual wall would prevent the tip from entering the silicone too far. The outline drawn on the monitor corresponded to a 40-mm diameter circle on the silicone and was meant to keep the rod's tip away from the sides of the Petri dish. Note that the instrument tip (and the subject's hands) moved in 3-D, but that the following plots are projected into 2-D.

Subjects were graduate students (ages 21–30, mean 26 years) who volunteered following a protocol approved by the University Human Subjects Committee. Before the trials, 12 min of training time were allowed, divided into 3 min for each of the Jacobian-based controllers. This length of training was deemed sufficient as subjects' actions after half a minute with a given controller were visually indistinguishable from their actions at the end of the training. After the training, subjects performed a 1 min trial for each controller, in the same order as the training. Between controllers, subjects were allowed to pause and stretch, and the silicone model was replaced. Ten subjects participated in this experiment, and the order of the controllers was counterbalanced between subjects. The position measurements from the magnetic tracker at the rod's tip were recorded during the trials to determine the depth the tip penetrated into the virtual fixture for each controller.

III. Results

For all subjects, the controller with both tip tracking and improved kinematics incurred least into the forbidden region (Fig. 8). The controllers with either tip tracking or improved kinematics incurred less often and less deeply than the controller with neither. The percentage of time each controller spent within the forbidden region was (mean $\pm$ standard deviation): Flex-Track 11% $\pm$ 5%, Straight-Track 32% $\pm$ 10%, Flex-Calculate 59% $\pm$ 13%, and Straight-Calculate 78% $\pm$ 10% (Fig. 9). Analysis of variance with repeated measures showed the differences in the controllers were significant at $p \leq 0.001$. The maximum depth each controller incurred into the forbidden region, measured across all subjects and trials, was: Flex-Track 1.0 $\pm$ 0.5 mm, Straight-Track 2.0 $\pm$ 1.0 mm, Flex-Calculate 4.3 $\pm$ 1.0 mm, and Straight-Calculate 6.0 $\pm$ 0.5 mm ($p \leq 0.001$) (Fig. 10).

The damage to the silicone inside the forbidden region was estimated in two ways. First, the trapezoidal rule was used to estimate the area between the virtual wall and pairs of temporally adjacent tip positions within the forbidden region. Averaged across subjects, these areas are: Flex-Track 39 $\pm$ 21 mm^2, Straight-Track 320 $\pm$ 330 mm^2, Flex-Calculate 1500 $\pm$ 610 mm^2, and Straight-Calculate 3400 $\pm$ 1100 mm^2 ($p \leq$ 0.001). Then, to prevent counting damage to the same piece of silicone more than once, the trajectories were projected onto two planes

Authorized licensed use limited to: Harvard University SEAS. Downloaded on July 8, 2009 at 15:59 from IEEE Xplore. Restrictions apply.

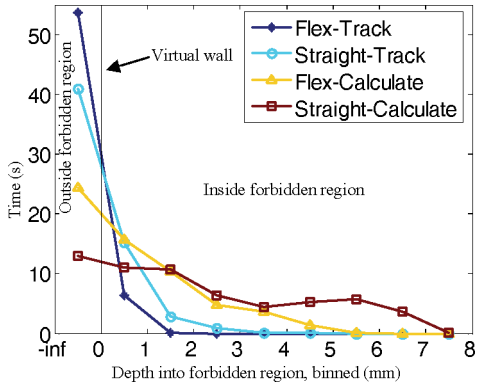

Fig. 9. Histogram of average time spent at various incursion depths. Straight-Calculate spends the most time inside the forbidden region, and has the deepest incursions.

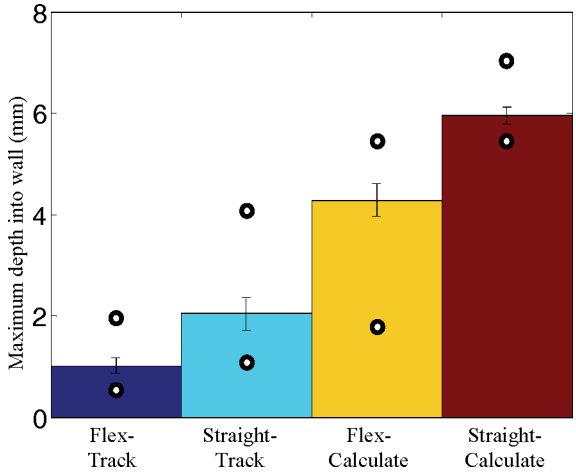

Fig. 10. Depth of maximum incursions per controller, averaged across all subjects. Lines show one standard error in either direction. Circles show minimums and maximums. All means significantly different at $p \leq 0.001$.

orthogonal to the virtual wall and to each other. For each of the two planes, the area within the outline of the projection was calculated. The two areas were summed together, and the averages across subjects demonstrated the same ordering with respect to controller: Flex-Track 15 ± 10 mm^2, Straight-Track 86 ± 81 mm^2, Flex-Calculate 230 ± 86 mm^2, and Straight-Calculate 352 ± 86 mm^2 ($p \leq 0.001$) (Fig. 11).

Figs. 12 and 13 show data from all the trials, with the subjects arbitrarily ordered with respect to maximum depth for the Straight-Calculate trials. Nine of the ten subjects had the same ordering of controllers both for time spent in the forbidden region (Fig. 12) and for maximum insertion depth (Fig. 13).

IV. Discussion

The goals of this work were to develop an image-guided system accurate in the presence of quasi-static kinematic changes that have been observed in robotic surgery, and to evaluate the separate benefits of two controller improvements. Both improvements, instrument tip tracking and an improved kinematic model, improved the motion accuracy of image-guided teleoperation involving a flexing instrument. Compared with the

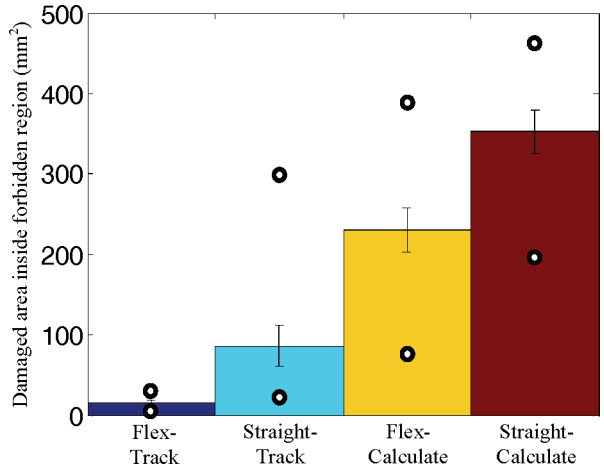

Fig. 11. Area calculated from union of trajectories projected onto orthogonal planes, averaged across all subjects. Lines show one standard error in either direction. Circles show minimums and maximums. All means significantly different at $p \leq 0.001$.

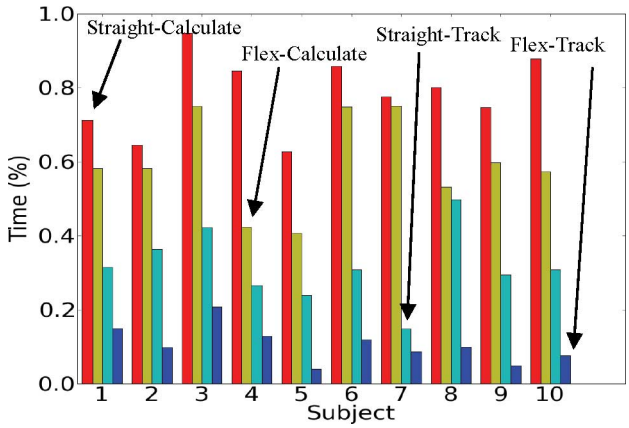

Fig. 12. Time spent in the forbidden region for each subject and each controller. For each subject, the controllers had the same order in terms of decreasing performance: Flex-Track, Straight-Track, Flex-Calculate, and Straight-Calculate.

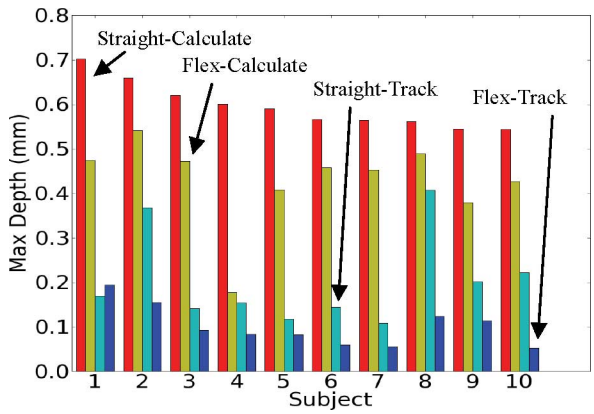

Fig. 13. Maximum depth incurred into the forbidden region for each subject and each controller. Subjects are ordered by maximum depth for the Straight-Calculate controller.

Authorized licensed use limited to: Harvard University SEAS. Downloaded on July 8, 2009 at 15:59 from IEEE Xplore. Restrictions apply.

controller using neither improvement, average reductions in the maximum incursion depth and the outlines of damaged area inside the forbidden region were 28% and 35% for flexed rod kinematics, 67% and 76% for tip tracking, and 83% and 96% for the combination of tip tracking and improved kinematics.

Tip tracking provided the largest reduction in the erroneous motions. Electromagnetic sensors were used in this experiment, but the proposed approach will also work with image-based tip feedback, e.g., from endoscopic video or biplane fluoroscopy. The magnitude of improvement will be dependent on the sensor's accuracy, noise characteristics, and susceptibility to target occlusion. Since the benefit of tip tracking is maximized by the use of a Jacobian-based controller, we would expect the advantage of tip tracking to be reduced if used with an inverse-kinematics-based controller.

The controller with flexion kinematics but not tip tracking performed better than the controller with neither improvement, but not as well as either controller with tip tracking. Its performance enhancement comes from improvements in the calculations of both the Jacobian and the tip position. These improvements are dependent on three factors: the agreement between the form of the model and the actual shaft geometries, the accuracy of the fit model parameters, and the registration accuracy between model coordinates and world coordinates. Like the benefits of tip tracking, these last two factors are dependent on the sensor capabilities. Even more than tip tracking, the parameter fit and registration are sensitive to sensor noise, e.g., small errors in wrist angle lead to large tip errors at the end of a long rod. As sensors improve, errors in the calculated tip position will decrease, closing the gap between this controller and the controllers with tip tracking. At a sufficient level of sensor accuracy and precision, the controller with flexion kinematics but not tip tracking would perform better than the controller with straight shaft kinematics and tip tracking.

The proposed model requires just two measurements to fit instrument flexion resulting from forces orthogonal to the instrument at the wrist, cannula, and tip. From the measurements, the instrument shape is modeled, the port position is determined, and the orientation of the instrument tip (and any cutting edge) is calculated. The forces used in the model were identified by observation during surgery as being the biggest cause of tip deflection. A more general flexion model would include instrument buckling due to axial forces, distributed forces caused by tissue interactions along the instrument, and a moment at the cannula caused by the incision site resisting cannula rotation. Experiments in the operating room will be necessary to evaluate the need for more complicated models that address such flexion sources. Additional sensors would be needed to fit the increased number of parameters, or could be used to reduce a simpler model's sensitivity to measurement noise.

The amount of information in a sensor modality affects the choice of controller. Current commercial electromagnetic sensors provide enough information to both track the instrument tip and to fit the flexion model; therefore, the controller with both tip tracking and flexion modeling can be used to maximize performance. The controllers with just tip tracking or just flexed rod kinematics are important because other sensing methodologies can provide only enough information for one enhancement or the other. For example, force sensors at the wrist and tip could provide measurements for fitting the flexion model's parameters, but cannot directly measure the tip position. Conversely, computer vision techniques could localize the tip position, but may not be able to measure the endpoint orientation with sufficient accuracy to fit the model parameters.

Though the "instrument" used in this experiment is not an actual surgical instrument, all surgical instruments experience some flexion to a degree determined by their geometry and loading. As surgeons attempt to reduce damage to healthy tissue and access smaller surgical targets, instrument diameters decrease and flexion increases correspondingly. The proposed controllers can reduce the errors of such flexion. In an attempt to avoid being limited to one instrument geometry, this discussion talks about the proportion of error reduction afforded by the proposed controllers instead of the absolute error magnitudes.

During the experiment, the silicone generated forces to resist motions of the instrument tip. Preliminary trials investigated several materials, including four different elastic moduli of silicone rubber and two different viscous clays. In those investigations, the material had little effect on the performance benefits observed between the four controllers. Silicone was used for this experiment because it is easily characterized and duplicated. The silicone's elastic modulus was relatively soft (3.4 kPa) because hard silicones tended to fracture suddenly, causing unrealistic dynamic oscillations as energy stored in the flexed instrument was released. The experimental results are a function of the instrument flexion, so the model's material is relatively insignificant as long as quasi-static instrument flexion occurs.

The best-performing controller in this experiment still entered the forbidden region due to measurement noise, model assumptions (e.g., small deflection linear theory), and shape changes between controller updates, which was limited to 144 Hz for the sensor used here. Port motions between sensor updates would result in an additional source of error in surgical settings, though it could be reduced by augmented models and additional sensors. To guide the instrument tip exactly along the boundary of the forbidden region, one of two modifications would be necessary. With a sufficiently fast sensor and controller update rate, the errors due to such unmodeled effects would be infinitesimal. Alternatively, the environment and instrument could be more accurately modeled, including the tissue response to a desired tip motion, instrument geometry changes between updates, and the port motion between updates.

Although virtual fixtures were used to demonstrate the motion errors in this experiment, applicability to particular surgical tasks will vary. Virtual fixtures used in soft tissue must, in general, account for tissue deformation due to interaction forces with the instrument, cuts, sutures, etc. Such adjustment can be made using real-time images [9] or through tissue models. In any case, reducing motion errors through the controller enhancements described in this paper will increase the usefulness of any autonomous or semiautonomous use.

The compensation techniques presented here are specialized for instrument tip interactions, i.e., tip penetration into tissue is small compared to the instrument length, which is typical in

Authorized licensed use limited to: Harvard University SEAS. Downloaded on July 8, 2009 at 15:59 from IEEE Xplore. Restrictions apply.

many laparoscopic and thoracoscopic procedures. With increasing penetration depth, the loading along the instrument shaft must be taken into account. This would require additional sensing and enhancement of the deflection model. The extreme case of continuous loading appears in the problem of needle driving, where elaborate methods have been proposed for controlling bending, including mechanical models of tissue deformation, real-time image processing to visualize the needle shape using fluoroscopy, determination of tissue mechanical properties, etc. [41]–[44]. In the long term, a "library" of diverse control modes might be used to enable accurate robot image guidance for thin instruments across a range of procedures. This paper proposes a first instance of one such technique, and the methodology here might serve as the basis for extensions to other cases of mechanical interactions.

The results of this experiment demonstrate the separate benefits of tip tracking and model-based error correction on accurate positioning in the presence of quasi-static flexion. Without these benefits, robot-assisted image guidance in surgery is hampered by errors in instrument motions, and by errors in the calculated instrument tip position. With these benefits, techniques such as virtual fixtures and augmented reality can accurately guide the surgeon.

REFERENCES

[1] M. Michael, D. Diodato, M. Sunil, M. Prosad, M. Mary, E. Klingensmith, M. Ralph, and J. Damiano, "Robotics in surgery," *Curr. Probl. Surg.*, vol. 41, pp. 752–810, 2004.

[2] R. H. Taylor and D. Stoianovici, "Medical robotics in computer-integrated surgery," *IEEE Trans. Robot. Autom.*, vol. 19, no. 5, pp. 765–781, Oct. 2003.

[3] K. Cleary and C. Nguyen, "State of the art in surgical robotics: Clinical applications and technology challenges," *Comput. Aided. Surg.*, vol. 6, no. 6, pp. 312–328, 2001.

[4] R. D. Howe and Y. Matsuoka, "Robotics for surgery," *Annu. Rev. Biomed. Eng.*, vol. 1, pp. 211–240, 1999.

[5] W. L. Bargar, A. Bauer, and M. Borner, "Primary and revision total hip replacement using the Robodoc system," *Clin. Orthop. Relat. Res.*, vol. 354, pp. 82–91, 1998.

[6] T. M. Peters, "Image-guidance for surgical procedures," *Phys. Med. Biol.*, vol. 51, pp. R505–R540, 2000.

[7] S. S. Park, R. D. Howe, and D. F. Torchiana, "Virtual fixtures for robot-assisted minimally-invasive cardiac surgery," in *Medical Image Computing and Computer-Assisted Intervention*, W. J. Niessen and M. A. Viergever, Eds. Berlin, Germany: Springer-Verlag, 2001, pp. 1419–1420.

[8] J. J. Abbott and A. M. Okamura, "Virtual fixture architectures for telemanipulation," in *Proc. IEEE Int. Conf. Robot. Autom.*, 2003, vol. 2, pp. 2798–2805.

[9] A. Bettini, P. Marayong, S. Lang, A. Okamura, and G. Hager, "Vision-assisted control for manipulation using virtual fixtures," *IEEE Trans. Robot.*, vol. 20, no. 6, pp. 953–966, Dec. 2004.

[10] J. Troccaz, M. A. Peshkin, and B. L. Davies, "The use of localizers, robots and synergistic devices in CAS," in *Proc. First Joint Conf. Comput. Vis. Virtual Reality Robot. Med. Medial Robot. Comput.-Assisted Surg.,* Springer Lecture Notes Computer Science, 1997, vol. 1205, pp. 727–736.

[11] H. Shennib, A. Bastawisy, M. J. Mack, and F. H. Moll, "Computer-assisted telemanipulation: An enabling technology for endoscopic coronary artery bypass," *Ann. Thorac. Surg.*, vol. 66, no. 3, pp. 1060–1063, 1998.

[12] E. R. Stephenson, Jr., S. Sankholkar, C. T. Ducko, and R. J. Damiano, Jr., "Robotically assisted microsurgery for endoscopic coronary artery bypass grafting," *Ann. Thorac. Surg.*, vol. 66, no. 3, pp. 1064–1067, 1998.

[13] E. Coste-Maniere, L. Adhami, F. Mourgues, and O. Bantiche, "Optimal planning of robotically assisted heart surgery: First results on the transfer precision in the operating room," *Int. J. Robot. Res.*, vol. 23, no. 4–5, pp. 539–548, 2004.

[14] A. M. Chiu, D. Dey, M. Drangova, W. D. Boyd, and T. M. Peters, "3-D image guidance for minimally invasive robotic coronary artery bypass," *Heart Surg. Forum.*, vol. 3, no. 3, pp. 224–231, 2000.

[15] F. Mourgues, T. Vieville, V. Falk, and È. Coste Manière, "Interactive guidance by image overlay in robot assisted coronary artery bypass," in *Proc. Med. Image Comput. Comput.-Assist. Intervention,* Springer Lecture Notes in Computer Science, 2003, vol. 2878, pp. 173–181.

[16] J. W. Cannon, J. A. Stoll, S. D. Selha, P. E. Dupont, R. D. Howe, and D. F. Torchiana, "Port placement planning in robot-assisted coronary artery bypass," *IEEE Trans. Robot. Autom.*, vol. 19, no. 5, pp. 912–917, Oct. 2003.

[17] C. R. Wagner, N. Stylopoulos, P. G. Jackson, and R. D. Howe, "The benefit of force feedback in surgery: Examination of blunt dissection," *Presence: Teleoper. Virtual Environ.*, vol. 16, no. 3, pp. 252–262, 2007.

[18] J. D. Brown, J. Rosen, L. Chang, M. Sinanan, and B. Hannaford, "Quantifying surgeon grasping mechanics in laparoscopy using the blue dragon system," *Med. Meet. Virtual Reality*, vol. 98, pp. 34–36, 2004.

[19] T. Kimura, S. Sakuramachi, M. Yoshida, T. Kobayashi, and Y. Takeuchi, "Laparoscopic cholecystectomy using fine-caliber instruments," *Surg. Endosc.*, vol. 12, no. 3, pp. 283–286, 1998.

[20] M. Li and R. H. Taylor, "Spatial motion constraints in medical robot using virtual fixtures generated by anatomy," in *Proc. IEEE Int. Conf. Robot. Autom.*, 2004, pp. 1270–1275.

[21] R. M. Sydorak and C. T. Albanese, "Minimal access techniques for fetal surgery," *World J. Surg.*, vol. 27, no. 1, pp. 95–102, 2003.

[22] M. Berris and M. Shoham, "Febotics—a marriage of fetal surgery and robotics," *Comput.-Aided Surg.*, vol. 11, no. 4, pp. 175–180, 2006.

[23] Y. Suematsu, J. F. Martinez, B. K. Wolf, G. R. Marx, J. A. Stoll, P. E. DuPont, R. D. Howe, J. K. Triedman, and P. J. del Nido, "Three-dimensional echo-guided beating heart surgery without cardiopulmonary bypass: Atrial septal defect closure in a swine model," *J. Thorac. Cardiovasc. Surg.*, vol. 130, no. 5, pp. 1348–1357, 2005.

[24] R. A. Beasley and R. D. Howe. (2005). Model-based correction for flexible robotic surgical instruments. *Robot.: Sci. Syst.* [Online]. vol. 1, pp. 359–364. Available: http://www.roboticsproceedings.org/rss01/p47.html

[25] C. Lee, Y.-F. Wang, D. R. Uecker, and Y. Wang, "Image analysis for automated tracking in robot-assisted endoscopic surgery," in *Proc. IAPR Int. Conf. Pattern Recognit., Conf. A: Comput. Vis. Image Proc.*, 1994, vol. 1, pp. 88–92.

[26] A. Casals, J. Amat, and E. Laporte, "Automatic guidance of an assistant robot in laparoscopic surgery," in *Proc. IEEE Int. Conf. Robot. Autom.*, 1996, vol. 1, pp. 895–900.

[27] G.-Q. Wei, K. Arbter, and G. Hirzinger, "Automatic tracking of laparoscopic instruments by color coding," in *Proc. Joint Conf. Comput. Vis. Virtual Reality Robot. Med. Med. Robot. Comput.-Assist. Surg.,* Lecture Notes in Computer Science, vol. 1205, 1997, pp. 357–366.

[28] A. Krupa, J. Gangloff, C. Doignon, M. F. de Mathelin, G. Morel, J. Leroy, L. Soler, and J. Marescaux, "Autonomous 3-D positioning of surgical instruments in robotized laparoscopic surgery using visual servoing," *IEEE Trans. Robot. Autom.*, vol. 19, no. 5, pp. 842–853, Oct. 2003.

[29] J. Climent and P. Mares, "Automatic instrument localization in laparoscopic surgery," *Electron. Lett. Comput. Vis. Image Anal.*, vol. 4, no. 1, pp. 21–31, 2004.

[30] M. Dewan, P. Marayong, A. Okamura, and G. Hager, "Vision-based assistance for ophthalmic micro-surgery," in *Proc. Med. Image Comput. Comput.-Assist. Intervention,* Lecture Notes in Computer Science, vol. 3217, 2004, pp. 49–57.

[31] M. S. Kim, J. S. Heo, and J. J. Lee, "Visual tracking algorithm for laparoscopic robot surgery," in *Fuzzy Systems and Knowledge Discovery,* vol. 3614. Berlin, Germany: Springer-Verlag, 2005, pp. 344–351.

[32] R. Riener, S. Reiter, M. Rasmus, D. Wetzel, and H. Feussner, "Acquisition of arm and instrument movements during laparoscopic interventions," *Minim. Invasive Ther. Allied Technol.*, vol. 12, no. 5, pp. 235–240, 2003.

[33] A. J. Chung, P. J. Edwards, F. Deligianni, and G. Yang, "Freehand cocalibration of optical and electromagnetic trackers for navigated bronchoscopy," *Med. Imag. Augmented Reality*, vol. 3150, pp. 320–328, 2004.

[34] M. Schneider and C. Stevens, "Development and testing of a new magnetic tracking device for image guidance," *Proc. SPIE Med. Imag.*, vol. 6509, 65090I, 2007.

[35] K. Schicho, M. Figl, M. Donat, W. Birkfellner, R. Seemann, A. Wagner, H. Bergmann, and R. Ewers, "Stability of miniature electromagnetic tracking systems," *Phys. Med. Biol.*, vol. 50, no. 9, pp. 2089–2098, 2005.

Authorized licensed use limited to: Harvard University SEAS. Downloaded on July 8, 2009 at 15:59 from IEEE Xplore. Restrictions apply.

[36] R. A. Beasley, R. D. Howe, and P. E. Dupont, "Kinematic error correction for minimally invasive surgical robots," in *Proc. IEEE Int. Conf. Robot. Autom.*, 2004, vol. 1, pp. 358–364.
[37] C. C. Cheah, M. Hirano, S. Kawamura, and S. Arimoto, "Approximate Jacobian control for robots with uncertain kinematics and dynamics," *IEEE Trans. Robot. Autom.*, vol. 19, no. 4, pp. 692–702, Aug. 2003.
[38] M. Shoham and Y. Koren, "Motion control algorithms for sensor-equipped robots," *J. Dyn. Syst., Meas. Control*, vol. 109, pp. 335–344, 1987.
[39] D. M. Rovner and R. H. Cannon, Jr., "Experiments toward on-line identification and control of a very flexible one-link manipulator," *Int. J. Robot. Res.*, vol. 6, no. 4, pp. 3–19, 1987.
[40] D.-S. Kwon and W. J. Book, "A time-domain inverse dynamic tracking control of a single-link flexible manipulator," *J. Dyn. Syst. Meas. Control*, vol. 116, pp. 193–200, 1994.
[41] S. P. DiMaio and S. E. Salcudean, "Needle insertion modeling and simulation," *IEEE Trans. Robot. Autom.*, vol. 19, no. 5, pp. 864–875, Oct. 2003.
[42] R. J. Webster, III, J. S. Kim, N. J. Cowan, G. S. Chirikjian, and A. M. Okamura, "Nonholonomic modeling of needle steering," *Int. J. Robot. Res.*, vol. 25, no. 5–6, pp. 509–525, 2006.
[43] D. Glozman and M. Shoham, "Image-guided robotic flexible needle steering," *IEEE Trans. Robot. Autom.*, vol. 23, no. 3, pp. 459–467, Jun. 2007.
[44] N. Abolhassani, R. V. Patel, and F. Ayazi, "Minimization of needle deflection in robot-assisted percutaneous therapy," *Proc. Int. J. Med. Robot. Comput. Assist. Surg.*, vol. 3, pp. 140–148, 2007.
[45] C. C. Cheah and H. C. Liaw, "Inverse Jacobian regulator with gravity compensation: Stability and experiment," *IEEE Trans. Robot.*, vol. 21, no. 4, pp. 741–747, Aug. 2005.
[46] T. J. Lardner and R. R. Archer, *Mechanics of Solids: An Introduction*. New York: McGraw-Hill, 1994, ch. 6, pp. 348–350.
[47] T. Belendez, C. Neipp, and A. Belendez, "Large and small deflections of a cantilever beam," *Eur. J. Phys.*, vol. 23, pp. 371–379, 2002.

Ryan A. Beasley (M'07) received the Bachelor's degrees in biomedical engineering and electrical engineering from Vanderbilt University, Nashville, TN, and the Ph.D. degree in engineering sciences from Harvard University, Cambridge, MA, in 2006.

He is currently an Assistant Professor of engineering technology and industrial distribution in the College of Engineering, Texas A&M University, College Station. His current research interests include surgical robotics, analog electronics, and artificial intelligence.

Robert D. Howe (S'88–M'89–SM'xx) received the Bachelor's degree in physics from Reed College, Portland, OR, and the Doctoral degree in mechanical engineering from Stanford University, Stanford, CA, in 1990.

He then was with the electronics industry in Silicon Valley. He is currently the Gordon McKay Professor of Engineering and Associate Dean for Academic Programs in the Harvard School of Engineering and Applied Sciences. He then joined the faculty at Harvard. He directs the Harvard BioRobotics Laboratory that investigates the roles of sensing and mechanical design in motor control, in both humans and robots. His current research interests focus on manipulation, the sense of touch, haptic interfaces, and robot-assisted and image-guided surgery.

Authorized licensed use limited to: Harvard University SEAS. Downloaded on July 8, 2009 at 15:59 from IEEE Xplore. Restrictions apply.